Chinese Chemical Letters 35 (2024) 108932

Contents lists available at ScienceDirect

Chinese Chemical Letters

journal homepage: www.elsevier.com/locate/cclet

Strong metal-support interaction between AuPd nanoparticles and oxygen-rich defect ZrO_2 for enhanced catalytic 5-hydroxymethylfurfural oxidation

Yunlei Zhang[a], Yiran Liu[a], Wen Guan[a], Mengxue Cao[a], Yao Chen[b,*], Pengwei Huo[a,*]

[a] Institute of Green Chemistry and Chemical Technology, School of Chemistry and Chemical Engineering, Jiangsu University, Zhenjiang 212013, China
[b] School of the Environment and Safety, Jiangsu University, Zhenjiang 212013, China

ARTICLE INFO

Article history:
Received 11 May 2023
Revised 25 July 2023
Accepted 13 August 2023
Available online 15 August 2023

Keywords:
5-Hydroxymethylfurfural oxidation
2,5-Furandicarboxylic acid
Oxygen-rich defect ZrO_2
AuPd bimetal
Bowl-shaped structure

ABSTRACT

The unique properties of metal oxide surfaces, crystal surfaces and defects play vital roles in biomass upgrading reactions. In this work, hierarchical porous bowl-shaped ZrO_2 (HB-ZrO_2) with mixed crystal phase was designed and employed as the support for loading AuPd bimetal with different proportions to synthesize AuPd/HB-ZrO_2 catalysts. The effects of surface chemistry, oxygen defects, bimetal interaction and metal-support interaction of AuPd/HB-ZrO_2 on catalytic performance for the selective oxidation of 5-hydroxymethylfurfural (HMF) to 2,5-furandicarboxylic acid (FDCA) were systematically investigated. The Au_2Pd_1/HB-ZrO_2 catalyst afforded a satisfactory FDCA yield of 99.9% from HMF oxidation using O_2 as the oxidant in water, accompanied with an excellent FDCA productivity at 97.6 mmol g^{-1} h^{-1}. This work offers fresh insights into rationally designing efficient catalysts with oxygen-rich defects for the catalytic upgrading of biomass platform chemicals.

Biomass resources have been listed as the fourth largest resource because of their abundant reserves, green and renewable characteristics [1]. As the only platform compound with aromatic ring among the 12 bio-based platform compounds promoted by the US Department of Energy, 5-hydroxymethylfurfural (HMF) derived from biomass is known as the "sleeping giant" [2,3]. HMF is centered on a unique furan ring and contains a hydroxymethyl group and an aldehyde group, which makes HMF rich in the development of thousands of downstream derivatives, including alcohols, acids, ethers, aldehydes, *etc.* [4,5]. The oxidation product of HMF, 2,5-furanediformic acid (FDCA) [6], has a structure similar to that of petrochemical derivative terephthalic acid (TPA), and can be polymerized with ethylene glycol to synthesize polyethylene 2,5-furanediformate (PEF) as an alternative to polyethylene terephthalate (PET). Compared with traditional PET, PEF has excellent gas barrier property, up to 6–10 times than that of PET, biodegradability can effectively alleviate the existing "white pollution" problem [7]. Therefore, it is urgent to develop an efficient catalytic system for the selective oxidation of HMF to produce FDCA.

Thermal catalysis [8], electrocatalysis [9,10], photocatalysis [11] and enzymatic catalysis [12] have been reported and exploited for the selective oxidation of HMF to FDCA. Heterogeneous catalysts are widely used in various reaction systems because of their easy separation, excellent stability and recyclability. The activation of oxygen plays a pivotal role in the process of oxidation reactions. The unique properties of the surface of metal oxides, crystal surfaces and defects can be regulated to enable the surface to have specific electronic or geometric properties as active centers to promote molecular activation. In addition, metal oxides are used as support for loading metal nanoparticles, and the interaction between the support and metals impacts the distribution and size of metal particles, thus producing different catalytic properties [13,14]. Metal oxide surfaces exhibit optimal activity and stability due to their high metal ion concentrations, oxygen vacancies (O_v) and exposure of multiple types of metal crystal faces [15]. Oxygen vacancies located near the metal perimeter and acted as preferential nucleation sites for metal nanoparticles loading. Moreover, the strong interaction between the nanoparticles and metal oxide support facilitates the acceleration of electron transfer from metal to the O_2 adsorbed at O_v of the support, thus improving catalytic activity that includes productivity and the turnover frequency (TOF) value. In previous studies, ZrO_2 with different crystalline phases (monoclinic, tetragonal and mixed phases) has been used as support to study a variety of reactions using its high thermal stability, tunable Brønsted-Lewis acidity and abundant sur-

* Corresponding authors.
E-mail addresses: chenyao1390@ujs.edu.cn (Y. Chen), huopw@ujs.edu.cn (P. Huo).

https://doi.org/10.1016/j.cclet.2023.108932
1001-8417/

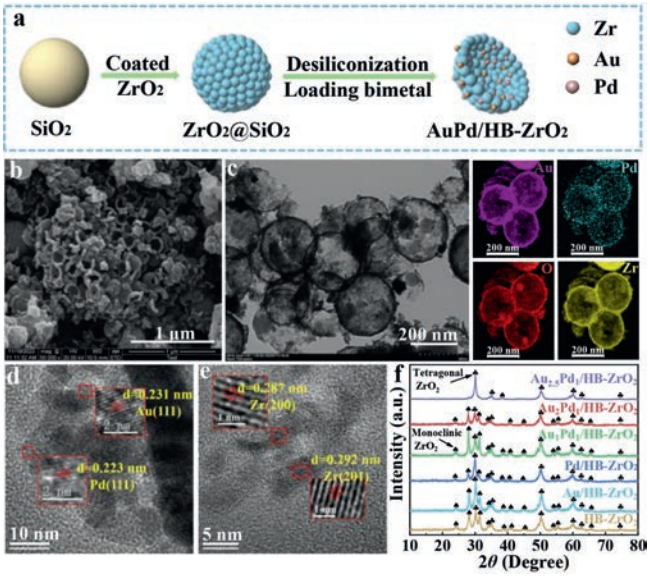

Fig. 1. The preparation process of AuPd/HB-ZrO_2 catalyst (a), SEM, TEM, EDS mapping and HRTEM images of Au_2Pd_1/HB-ZrO_2 (b–e), XRD patterns of AuPd/HB-ZrO_2 (f).

face defects [15–18]. ZrO_2 with different crystalline phases supported metals were synthesized and employed for catalytic oxidation of toluene. The results revealed that Pt/ZrO_2 with mixed phase possessing better catalytic activity than that of Pt/ZrO_2 with monoclinic phase, and the strong interaction between metal and support played an important role in the oxidation process of toluene [19]. The O_v induced strong metal-support interaction on Au/ZrO_2 catalysts was rationally designed, and the generated interface active sites between metal and support can be tuned and employed for the high-efficient aerobic oxidation of HMF to FDCA [20]. This strategy sheds light on the design of oxygen-rich defect metal oxide supported-metal catalysts for the related biomass oxidation reactions.

Herein, SiO_2 nanospheres were used as template to prepare hierarchical porous bowl-shaped ZrO_2 (HB-ZrO_2) with mixed crystal phase and employed as the support for loading AuPd bimetal with different proportions to synthesize AuPd/HB-ZrO_2 catalysts (Fig. 1a). The optimal Au_2Pd_1/HB-ZrO_2 catalyst exhibited the highest FDCA yield (99.9%) with complete HMF conversion. The SEM and TEM images (Figs. 1b and c) of Au_2Pd_1/HB-ZrO_2 showed that the bowl-shaped ZrO_2 support was composed of uniform ZrO_2 pellets, and the subsequent loading of AuPd metal particles did not affect the morphology of the support (Figs. S1 and S2 in Supporting information). The EDS mapping of Au_2Pd_1/HB-ZrO_2 exhibited the uniform loading of Au and Pd particles on the surface of HB-ZrO_2 support. As shown in Figs. 1d and e, HRTEM images of Au_2Pd_1/HB-ZrO_2 presented characteristic crystal plane spacing of Au (111) and Pd (111). The lattice spacing was 0.287 and 0.292 nm, which falls into the range of the d-spacings of tetragonal ZrO_2 (200) and tetragonal ZrO_2 (201) (JCPDS No. 79–1764). The X-ray diffraction (XRD) patterns of the catalysts with different Au-Pd ratios were exhibited in Fig. 1f. The HB-ZrO_2 support presented a mixture of monoclinic and tetragonal zirconia crystalline phases, in which the peaks at 2θ positions 24.2°, 28.2°, 31.4°, 34.1°, 38.5°, 40.8°, 45.1°, 54.1°, 55.4° and 65.6° were ascribe to the monoclinic phase (JCPDS No. 37–1484), while 30.1°, 35.0°, 50.2°, 60.1°, 62.8° and 74.5° were assigned to the tetragonal phase (JCPDS No. 79–1764). After loading AuPd nanoparticles, the characteristic diffractions of HB-ZrO_2 support were observed as the main diffraction for all samples due to the relatively low contents and small size of metal nanoparticles, and their characteristic diffractions were masked by the characteristic diffractions of zirconia. Different proportions of Au and Pd interact with the support differently. When the ratio of Au to Pd was 1:0, the weak interaction force between the HB-ZrO_2 support and Au nanoparticles resulted in the aggregation of Au nanoparticles (Fig. S2b). With the change of Au and Pd ratio, the interaction force between metal particles and the HB-ZrO_2 support became stronger, resulting in the uniform distribution of metal particles on the surface of the HB-ZrO_2 support. When the ratio of Au to Pd increased to 2.5:1, the crystalline phase of the catalyst was mainly tetragonal ZrO_2. The nitrogen adsorption and desorption tests revealed that the specific surface area of the catalyst decreased, while the average pore diameter increased with the change of AuPd ratio (Table S1 and Fig. S3 in Supporting information). In particular, due to the small size of palladium particles, the specific surface area did not change significantly, and the average pore diameter represented a decrease trend.

The surface chemical properties of the catalysts were analyzed by XPS surface characterization of Au/HB-ZrO_2, Pd/HB-ZrO_2, and Au_2Pd_1/HB-ZrO_2. Compared with the standard binding energies of Au $4f_{7/2}$ (BE = 84.0 eV) and Au $4f_{5/2}$ (BE = 87.7 eV) [21], the binding energies of Au $4f_{7/2}$ and Au $4f_{5/2}$ that ascribed to Au^0 for Au/HB-ZrO_2 and Au_2Pd_1/HB-ZrO_2 were negatively shifted (0.2 eV). Binding energies at 86.8 and 90.0 eV indicated the presence of Au^{3+} (Fig. 2a). In the XPS spectra of Pd 3d (Fig. 2b), the binding energies of Pd/HB-ZrO_2 and Au_2Pd_1/HB-ZrO_2 in Pd 3d region also shifted significantly in relation to Pd^0 and Pd^{2+} [22], indicating the formation of alloyed AuPd nanoparticles. The Zr 3d region of HB-ZrO_2 and AuPd/HB-ZrO_2 (Fig. S4 in Supporting information) demonstrated that Zr species were mainly Zr^{3+} and Zr^{4+} [23]. In particular, compared with HB-ZrO_2, the binding energies of Zr $3d_{5/2}$ of Au/HB-ZrO_2 and Pd/HB-ZrO_2 were negatively shifted, but the binding energies of O 1s of Pd/HB-ZrO_2 were positively shifted (Fig. 2c and Fig. S4). According to the XPS results, the interaction between the O_v and the metallic center involves electron transfer from the structural defects from HB-ZrO_2 support toward AuPd nanoparticles, suggesting O_v acted as preferential nucleation sites for AuPd nanoparticles loading. At the same time, in the XPS spectra of O 1s, AuPd/HB-ZrO_2 revealed that oxygen species was the oxygen species bonded weakly to the catalyst surface (O_{others}: OH^-, CO_3^{2-} or adsorbed molecular H_2O), adsorbed oxygen (O_{ads}) and surface lattice oxygen (O_{latt}) [15]. The concentration and peak position of oxygen species on the surface of ZrO_2 were shifted obviously with different metal loads. In the O 1s map of Au/HB-ZrO_2, the characteristic peak of oxygen species $O_{others,}$ $O_{ads,}$ and O_{latt} shifted to the lower energy level. The oxygen species $O_{others,}$ $O_{ads,}$ and O_{latt} characteristic peak of Pd/HB-ZrO_2 shifted to higher energy level. The oxygen species characteristic peak of Au_2Pd_1/HB-ZrO_2 was only slightly different from that of HB-ZrO_2. XPS data exhibited in Fig. 2 and Fig. S4 suggested that substantial increases in the concentration of the O_v and Zr^{3+} state caused by the loading of AuPd bimetal on HB-ZrO_2 support, resulting in strong metal-support interaction.

The surface defects of catalysts were studied by EPR technique (Fig. 2d). Compared with the peak intensity of different catalysts, the relative intensity of Au_2Pd_1/HB-ZrO_2 was the strongest, and the result matched well with the XPS characterization that loading the bimetal increases the O_v concentration of the HB-ZrO_2 support. NH_3 temperature-programmed desorption (TPD) was carried out to investigate the concentration and distribution of acid sites over HB-ZrO_2 supported mono-metal and bimetallic catalysts (Fig. S5a in Supporting information). The acid sites were detected for all three catalysts in the range of weak acid (100–200 °C) and strong acid (350–600 °C) [15]. The Au_2Pd_1/HB-ZrO_2 catalyst revealed the highest acid strength. By pyridine infrared spectroscopy (Fig. 2e), the characteristic peak at 1446 cm^{-1} was corresponded to the co-

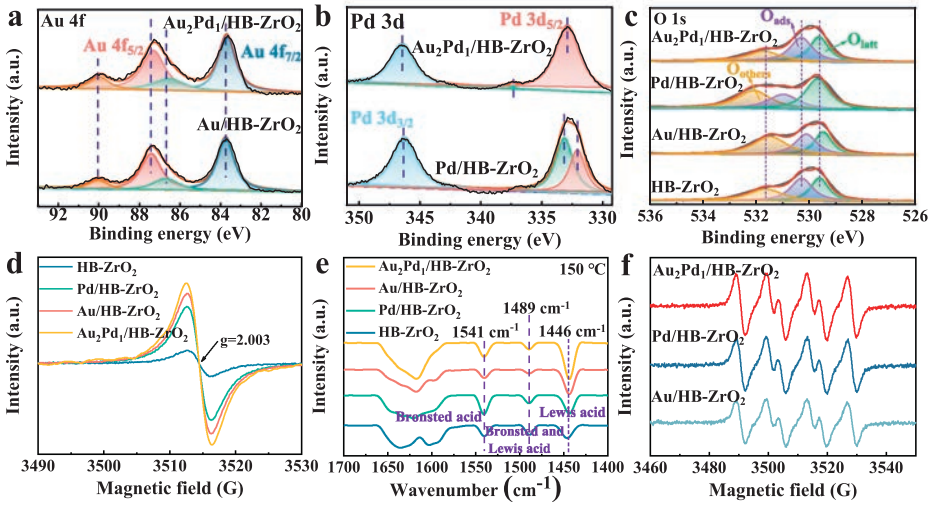

Fig. 2. The XPS spectra of Au 4f (a), Pd 3d (b), and O 1s (c) of AuPd/HB-ZrO_2, EPR spectra of AuPd/HB-ZrO_2 (d), FTIR-pyridine adsorption of AuPd/HB-ZrO_2 (e), ESR spectra of AuPd/HB-ZrO_2 (f).

ordination between pyridine and Lewis acid sites. The characteristic peak at 1541 cm^{-1} was attributed to the adsorption of pyridine on the Brønsted acid site, and the characteristic band at 1489 cm^{-1} was ascribed to the adsorption overlap of pyridine on the Lewis and Brønsted acid sites [24]. Compared with HB-ZrO_2 support, the intensity of Lewis acid exhibited substantial increases after loading metal nanoparticles. And the Au_2Pd_1/HB-ZrO_2 catalyst showed stronger Lewis acid than the other three samples, suggesting more O_v concentration was induced by AuPd bimetal. The results were consistent with those obtained by EPR and NH_3-TPD. O_2-TPD was used to further explore the oxygen species adsorbed on the catalyst surface (Fig. S5b in Supporting information). The low temperature region (100–250 °C) was known to be the physical adsorbed oxygen region, the middle temperature region (250–600 °C) was the adsorbed oxygen region associated with oxygen vacancy, and the high temperature region (600–800 °C) was the bulk lattice oxygen release region [25]. It can be seen from Fig. S5b, Au_2Pd_1/HB-ZrO_2 has various oxygen absorption peaks, and the O_v-related adsorption oxygen peak was stronger, so it was speculated that there are more O_v sites for the adsorption and activation of O_2. The ESR test observed that Au_2Pd_1/HB-ZrO_2 catalyst presented a stronger ESR signals of DMPO-$^{\bullet}O_2^-$ than that of the other synthesized catalysts (Fig. 2f). Overall, the characterizations results revealed the strong metal-support interaction between AuPd nanoparticles and HB-ZrO_2 support that benefited adsorption and activation of O_2.

The catalytic performance of the prepared catalysts for the oxidation of HMF to FDCA was investigated at 100 °C, 2.0 MPa O_2 for 660 min. 5-Hydroxymethyl-2-furancarboxylic acid (HMFCA), 5-formyl-2-furancarboxylic acid (FFCA) and FDCA intermediates were detected during the reaction, but no 2,5-diformylfuran (DFF) was found, suggesting that the reaction process followed path: HMF-HMFCA-FFCA-FDCA. In addition, the oxidation of HMF to FDCA employing HB-ZrO_2 that free of metals as catalyst revealed that only small amounts of HMFCA and FFCA were observed, and the final FDCA product was not detected in 300 min (Fig. S6 in Supporting information), indicating AuPd bimetal was the active site for FDCA production. After 5 min of reaction time, HMF conversion reached 100% and the yield of FDCA was 50.2% (Fig. 3a). The yield of FDCA was 99.9% with 97.6 mmol g^{-1} h^{-1} productivity after 300 min reaction. The effect of the mole ratios of Au and Pd in the bimetallic catalyst was tested. The monometallic catalysts Au/HB-ZrO_2 and Pd/HB-ZrO_2 showed 55.2% (52.5 mmol g^{-1} h^{-1}) and 20.2% (18.7 mmol g^{-1} h^{-1}) FDCA yields at 300 min with com-

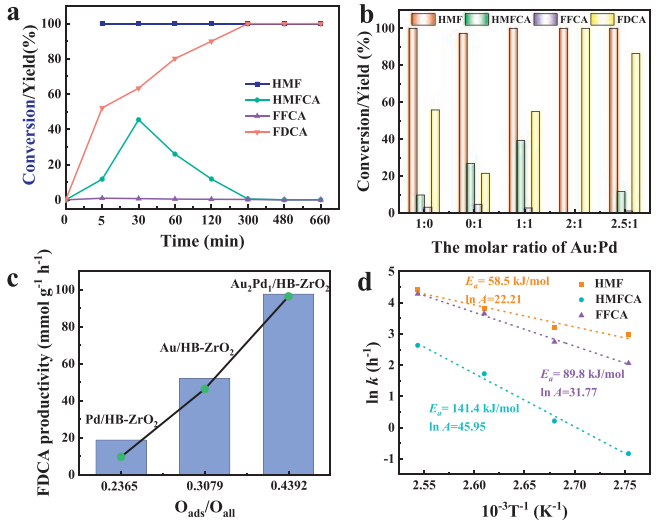

Fig. 3. The time course of HMF conversion, intermediate and final product yields over Au_2Pd_1/HB-ZrO_2 (a), the influences of the mole ratios of Au and Pd on the catalytic performance over AuPd/HB-ZrO_2 (b), the relationship between O_v content and FDCA productivity (c) (Reaction conditions: 100 °C, 2.0 MPa oxygen, n(NaOH)/n(HMF) = 4:1, 50 mg of catalyst loading), the arrhenius plots of ln k based on different temperatures (d).

plete conversion of HMF, respectively (Fig. 3b, Fig. S7a in Supporting information). When the molar ratio of Au and Pd was adjusted to be 1:1, the yield of FDCA was significantly improved at the initial stage of reaction, but only 55.1% of FDCA yield can be achieved (48.3 mmol g^{-1} h^{-1}) at 300 min. Further increasing the molar ratio of Au to Pd to be 2:1, the Au_2Pd_1/HB-ZrO_2 catalyst exhibited the best catalytic performance, and the yield of FDCA reached 99.9%. The yield of FDCA decreased with the increasing molar ratio of metal. It was concluded that the optimal molar ratio of Au and Pd was 2:1. At the same time, the yield of FDCA was positively correlated with the oxygen defect content of catalyst (Fig. 3c). In order to further verify the effect of reaction temperature, catalytic tests were carried out under different temperature conditions (Fig. S7b in Supporting information). The results showed that the yield of FDCA can reach 99.9% at 100 °C, and the increase of reaction temperature has no obvious effect on the system. Studies have shown that O_2 played a role in removing electrons from metal surface

during HMF oxidation, speeding up the electron transport rate in the reaction process, and promoting the adsorption and dehydrogenation of hydroxide ions [26,27]. Under the condition of 0.5 MPa oxygen pressure, the yield of FDCA was 78.5% (74.0 mmol g^{-1} h^{-1}). With the increase of oxygen pressure, FDCA yield of 99.9% was obtained at 2.0 MPa (Fig. S7c in Supporting information). When the amount of catalyst was 30 mg, the yield of FDCA was 50.1% (78.8 mmol g^{-1} h^{-1}), and further increasing the catalyst amount to 50 mg achieved the highest yield of 99.9% (Fig. S7d in Supporting information). Recyclability test of Au_2Pd_1/HB-ZrO_2 showed that the catalyst maintained good stability and the yield of FDCA only decreased by 5% after 5 cycles, which was mainly caused by the agglomeration of supported AuPd bimetal nanoparticles. (Fig. S8 in Supporting information).

According to the generated intermediates during the reaction process, the reaction process followed the sequence of HMF-HMFCA-FFCA-FDCA over Au_2Pd_1/HB-ZrO_2. Kinetics studies were carried out to calculate the apparent activation energies (E_a), and the results indicated the HMFCA oxidation demanded higher E_a than that of HMF substrate and FFCA (Fig. 3d and Tables S2–S4 in Supporting information). In the time course of HMF conversion, intermediate and FDCA yields in Fig. 3a also indicated that the HMF substrate swiftly converted and the HMFCA yield kept at a higher level than FFCA, suggesting that the oxidation of HMFCA should be the rate-determining step during HMF oxidation. The adsorption capacities of HMFCA over three catalysts were studied. After Langmuir and Freundlich isothermal adsorption model fitting, the HMFCA adsorption processes of the three catalysts were well fitted to the Langmuir model, indicating that the adsorption process of HMFCA was monolayer adsorption (Fig. S9 in Supporting information). According to Langmuir isothermal adsorption linear equation, the maximum adsorption capacity of Au_2Pd_1/HB-ZrO_2 for HMFCA was 1.1832 mg/g. The *n* value obtained by Freundlich isothermal adsorption linear equation was associated with the adsorption strength. Three catalysts were all favorable for the adsorption of HMFCA, and Au_2Pd_1/HB-ZrO_2 had the best adsorption effect (Table S5 in Supporting information). The catalytic performance of this developed catalyst was superior to supported catalysts for HMF oxidation in the reported literatures (Table S6 in Supporting information).

Control experiment indicated alkaline condition was essential for the catalytic oxidation of HMF to FDCA over the developed Au_2Pd_1/HB-ZrO_2 catalyst (Fig. S10 in Supporting information). In addition, the *in situ* infrared adsorption experiments revealed that HMF was vertically adsorbed on Au_2Pd_1/HB-ZrO_2 catalyst surface (Fig. S11 in Supporting information). Based on catalysts characterizations and catalytic activities, the possible reaction mechanism of HMF conversion to FDCA under the action of Au_2Pd_1/HB-ZrO_2 catalyst was speculated as illustrated in Fig. 4. The hydroxyl group of HMF was adsorbed on the catalyst, and activated by the active precious metal on the surface. The oxygen vacancy adsorbed and activated O_2 to form $^{\bullet}O_2^-$. Meanwhile, the aldehyde group on HMF was formed into geminal diols [28,29]. The geminal diols were further combined with OH^- to form HMFCA. HMFCA was activated by metal and continued to react with OH^- to form FFCA. FFCA hydrolyzed to form intermediates, which further form FDCA under the action of metals and OH^-. The synergistic action between the metal oxide support as the oxidation terminal and the metal particle as the reduction terminal accelerated the electron transfer rate in the reaction process, and finally realized the catalytic oxidation of HMF to FDCA.

In summary, hierarchical porous bowl-shaped ZrO_2 with oxygen-rich defect was designed and employed as AuPd bimetal nanoparticles support for high-efficient oxidation of HMF to FDCA. Compared with Au/HB-ZrO_2 and Pd/HB-ZrO_2 catalysts, AuPd/HB-ZrO_2 catalysts with bimetallic nanoparticles loading induced more

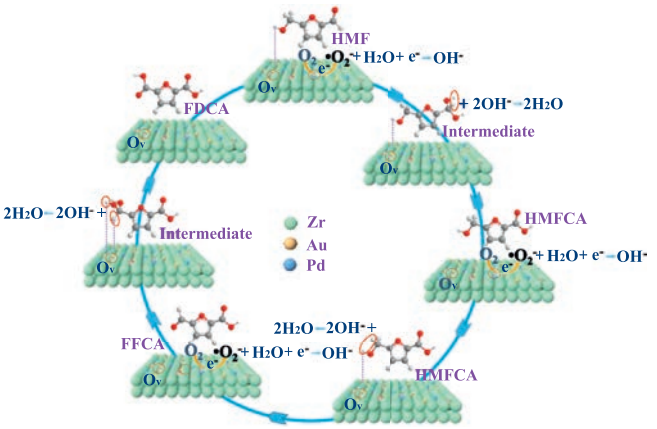

Fig. 4. Proposed mechanism of HMF tandem oxidation to FDCA over the Au_2Pd_1/HB-ZrO_2 catalyst.

O_v content, thus resulting in enhanced strong metal-support interaction. The O_v on the surface of HB-ZrO_2 was conducive to the dissociation of oxygen, and further removed the electrons transmitted to the surface of metal particles, accelerated the electron transfer rate in the reaction process. The Au_2Pd_1/HB-ZrO_2 catalyst afforded a satisfactory FDCA yield of 99.9%, accompanying with an excellent FDCA productivity at 97.6 mmol g^{-1} h^{-1}. Moreover, kinetic studies confirmed the rate-determining step was the oxidation of HMFCA to FFCA during HMF oxidation over the Au_2Pd_1/HB-ZrO_2 catalyst. This work sheds new lights on the design of well-controlled metal oxide supported noble metal catalysts for the catalytic upgrading of biomass platform chemicals.

Declaration of competing interest

The authors declare that they have no known competing financial interests or personal relationships that could have appeared to influence the work reported in this paper.

Acknowledgments

This work was financially supported by the Natural Science Foundation of Jiangsu Province (No. BK20200917), the China Postdoctoral Science Foundation (No. 2021M701474), Youth Talent Cultivation Plan of Jiangsu University, and Collaborative Innovation Center for Water Treatment Technology and Materials.

Supplementary materials

Supplementary material associated with this article can be found, in the online version, at doi:10.1016/j.cclet.2023.108932.

References

[1] N. Chi Van, D. Lewis, W.H. Chen, et al., Catal. Today 278 (2016) 344–349.
[2] F. Menegazzo, E. Ghedini, M. Signoretto, Molecules 23 (2018) 2201.
[3] T. Wang, M.W. Nolte, B.H. Shanks, Green Chem. 16 (2014) 548–572.
[4] M. Sun, Y. Wang, C. Sun, et al., Chin. Chem. Lett. 33 (2022) 385–389.
[5] Z. Jiang, Y. Zeng, D. Hu, et al., Green Chem. 25 (2023) 871–892.
[6] P. Pal, S. Saravanamurugan, ChemSusChem 12 (2019) 145–163.
[7] J.B. Heo, Y.S. Lee, C.H. Chung, Biotechnol. Adv. 53 (2021) 107838.
[8] C. Chen, L. Wang, B. Zhu, et al., J. Energy Chem. 54 (2021) 528–554.
[9] Y. Zhao, M. Cai, J. Xian, Y. Sun, G. Li, J. Mater. Chem. A 9 (2021) 20164–20183.
[10] O. Simoska, Z. Rhodes, S. Weliwatte, et al., ChemSusChem 14 (2021) 1674–1686.
[11] Y. Meng, S. Yang, H. Li, ChemSusChem 15 (2022) e202102581.
[12] D. Haldar, D. Sen, K. Gayen, Int. J. Green Energy 13 (2016) 1232–1253.
[13] S. Albonetti, T. Pasini, A. Lolli, et al., Catal. Today 195 (2021) 120–126.
[14] Z. Gao, R. Xie, G. Fan, L. Yang, F. Li, ACS Sustain. Chem. Eng. 5 (2017) 5852–5861.
[15] Y. Zhou, L. Liu, G. Li, C. Hu, ACS Catal. 11 (2021) 7099–7113.

[16] B. Liu, S. Xu, M. Zhang, et al., Green Chem. 23 (2021) 4034–4043.
[17] H.K. Min, Y.W. Kim, C. Kim, et al., Chem. Eng. J. 428 (2022) 131766.
[18] Y. Zheng, M. Okumura, X. Hua, et al., J. Catal. 401 (2021) 188–199.
[19] X. Yang, X. Ma, X. Yu, M. Ge, Appl. Catal. B: Environ. 263 (2020) 118355.
[20] Y. Zhang, Y. Cao, C. Yan, et al., Chem. Eng. J. 459 (2023) 141644.
[21] M.P. Casaletto, A. Longo, A. Martorana, A. Prestianni, A.M. Venezia, Surf. Interface Anal. 38 (2006) 215–218.
[22] F. Jiang, S. Wang, B. Liu, et al., ACS Catal. 10 (2020) 11493–11509.
[23] W. Li, Y. Liu, M. Mu, et al., Appl. Catal. B: Environ. 254 (2019) 531–540.
[24] Q. Li, H. Wang, Z. Tian, et al., Catal. Sci. Technol. 9 (2019) 1570–1580.
[25] H. Zhang, T. Gao, Q. Cao, W. Fang, ACS Sustain. Chem. Eng. 9 (2021) 6056–6067.
[26] B.N. Zope, D.D. Hibbitts, M. Neurock, R.J. Davis, Science 330 (2010) 74–78.
[27] V.R. Gangwal, J. van der Schaaf, B.F.M. Kuster, J.C. Schouten, J. Catal. 229 (2005) 389–403.
[28] G. Wu, G. Zhao, J. Sun, et al., J. Catal. 377 (2019) 271–282.
[29] Y. Pan, G. Wu, Y. He, J. Feng, D. Li, J. Catal. 369 (2019) 222–232.